A comparative study between AZ31 and Mg-Gd alloys after high-pressure torsion

Ouarda Ould Mohamed[1], Piotr Bazarnik[2], Yi Huang[3,4], Hiba Azzeddine[1,*], Thierry Baudin[5], François Brisset[5], Terence G. Langdon[3]

[1] Laboratory of Materials and Renewable Energy, Faculty of Sciences, Mohamed Boudiaf University, 28000 M'sila, Algeria

[2] Warsaw University of Technology, Faculty of Materials Science and Engineering, Woloska 141, 02-507, Poland

[3] Materials Research Group, Department of Mechanical Engineering, University of Southampton, Southampton SO17 1BJ, UK

[4] Department of Design and Engineering, Faculty of Science and Technology, Bournemouth University, Poole, Dorset BH12 5BB, UK

[5] Université Paris-Saclay, CNRS, Institut de chimie moléculaire et des matériaux d'Orsay, 91405 Orsay, France

* Corresponding author: Prof. Hiba Azzeddine, hiba.azzeddine@univ-msila.dz

Abstract

The evolution of microstructure, texture, and mechanical properties of AZ31 (Mg-3Al-1Zn, wt.%) and Mg-0.6Gd (wt.%) alloys were investigated and compared after high-pressure torsion at room temperature through the equivalent strain range of ε_{eq} = 0.6-287.5. The results demonstrated that the grain refinement behavior is different for these two alloys. For the AZ31 alloy, dynamic recrystallization (DRX) was restricted leading to a gradual and continuous formation of ultrafine grains with a mean grain size of ~0.3 µm through the entire strain range and the development of deviated B, C_1, and C_2 texture fibers. For the Mg-0.6Gd alloy, the DRX was very fast and a rapid ultrafine grain microstructure with a mean grain size of ~0.7 µm was developed at a strain range of ε_{eq} = 0.6-5.7 and this remained stable with a relatively stable B-fiber over the strain range ε_{eq} = 5.7-287.5. The evolution of microhardness in the AZ31 alloy indicated a strain hardening without recovery while that of the Mg-0.6Gd alloy showed a strain hardening with recovery. The differences between the AZ31 and Mg-0.6Gd alloys are discussed based on a comprehensive characterization of twinning, dislocation density, the initial microstructure and the presence of second phases.

Keywords: Dynamic recrystallization; High-pressure torsion; Magnesium; Microstructure; Rare-earth; Texture

1. Introduction

Magnesium (Mg) and its alloys have great potential to be used in diverse industries including transportation, electronic and biomedical owing to their attractive physical and chemical properties such as low density, high strength, recyclability, and biocompatibility [1-4]. However, the formability of Mg-based alloys is very limited at room temperature (RT) because of the lack of sufficient active slip systems and the development of sharp basal texture which is due to the hexagonal close-packed structure of Mg [5]. The deformation at low temperatures is accommodated by the basal <a> slip system and the mechanical twinning generally known as {10-11}<10-12> contraction and {10-12}<10-11> extension twins owing to their low critical resolved shear stress (CRSS) values [6, 7]. The activation of non-basal slip systems like <c+a> pyramidal slip which can accommodate strain along the c-axis is hard due to its high CRSS value which is ~80 times larger than that of <a> basal slip in pure Mg [8]. The promotion of <c+a> pyramidal slip system by decreasing the CRSS value may be achieved by changing the alloying elements [9] or increasing the deformation temperature [10].

It follows therefore that the mechanical properties of Mg-based alloys can be tailored by chemical composition and by processing technologies [11]. The improvement of mechanical properties of Mg alloyed with rare-earth (RE) elements is usually related to solute strengthening, fine-grain strengthening and precipitation strengthening [12]. In addition, one of the benefic effects of adding RE elements is the modification of texture which leads to a weakening of the basal texture by comparison to the traditional AZ-based alloys which has a direct effect on improving the ductility and decreasing the anisotropy of the Mg-RE alloys [13-17].

Conventional thermomechanical processing, which is a combination of deformation and heat treatment, is an excellent tool for controlling the microstructures and mechanical properties of Mg-based alloys. In such conditions, the mechanical improvement is related to grain refinement owing to the activation of non-basal slip systems and the occurrence of dynamic recrystallization (DRX) [18-25]. According to the nature of the recrystallization process, Discontinuous DRX (DDRX) and Continuous DRX (CDRX) are the main mechanisms responsible for DRX in Mg-based alloys [26]. DDRX mechanism is characterized by nucleation and a growth process and usually the formation of recrystallized grains occurrences along the grain boundaries [26]. In the CDRX mechanism, the formation of recrystallized new grains is due to the continuous absorption of dislocations in sub-grain boundaries which progressively transform into low-angle grain boundaries (LAGBs) and then into high-angle grain boundaries

(HAGBs) [26]. The CDRX mechanism dominates when the initial material exhibits coarse grains while DDRX dominates in deformed material with initial fine grains [27, 28]. It is reported that the CDRX mechanism is characterized by slow kinetics and requires larger strains than the DDRX mechanism [29].

Among the new severe plastic deformation (SPD) techniques, high-pressure torsion (HPT) has become an established processing procedure that is used extensively for achieving remarkable grain refinement and superior properties in a range of different metals [30, 31]. Furthermore, the HPT process is at present the only SPD technique that allows Mg-based metals to be deformed conveniently at room temperature (RT) [32-36]. Indeed, HPT processing was successfully applied at RT to fabricate a novel hybrid material from separate discs of the AZ31 (Mg-3Al-1Zn, wt.%) and Mg-0.6Gd (wt.%) alloys [37]. It is recognized that grain refinement is governed by the CDRX mechanism in SPD-processed materials at RT or warm temperatures [29, 38].

Several reports show that the DRX in Mg-RE alloys is retarded or restricted due to the easy activation of non-basal slip systems so that DRX is not required to accommodate the deformation [24, 25, 39]. By contrast, it was reported that the improvement in formability of Mg-Gd alloys is related to a change in the recrystallization behaviour and the resulting texture rather than the activation of supplementary slip systems [40]. There has been significant research focusing on highlighting the differences in deformation behaviour, microstructure, and texture evolution under conventional thermomechanical processing between pure Mg or the traditional AZ31 alloy and Mg-RE alloys [40-45]. For example, the stored energy was lower for AZ31 than the Mg-1.5Gd (wt.%) alloy under hot plane strain compression for a true strain of 0.7 [41]. Consequently, the static recrystallization kinetics of the Mg-1.5Gd alloy was notably faster than the AZ31 alloy [42].

It is important to note that similar comparison studies are not yet available for HPT-processed Mg-based alloys. Therefore, the present work was designed specifically to compare the evolution of the microstructure, texture and microhardness of AZ31 and Mg-0.6Gd (wt. %) alloys separately processed by HPT at RT for an equivalent strain range of ε_{eq} = 0.6-287.5.

2. Experimental materials and procedures

Sheets of a hot-rolled AZ31 alloy and an as-cast Mg-0.6Gd alloy were provided by the Magnesium Innovations Center (MagIC, Germany) and the Institute of Physical Metallurgy and Materials Physics (RWTH-Aachen University, Germany), respectively. Accordingly, the Mg-

0.6Gd alloy was fabricated by induction melting and casting under a protective gas of Ar/CO_2 using preheated copper mold. Then, the as-cast alloy was subjected to heat treatment for 20 h at 420 °C.

The HPT processing was performed on discs with diameters of 10 mm and thicknesses of 0.85 mm at room temperature for N = 1/2, 5, 10 and 20 turns under quasi-constrained conditions [46]. The disc samples were processed under a pressure of 6.0 GPa with a rotational speed of 1 rpm. In quasi-constrained HPT processing, the two anvils are separated so that there is always a minor outflow of material around the periphery of the disc during processing and this causes a decrease in the thickness of the disc which was from 0.85 to 0.63 mm in the present experiments.

The microstructure and texture analyses were taken on the cross-sectional (CD-RD) planes of the HPT discs where the shear reference frame is defined as the radial direction (RD), compression direction (CD) and shear direction (SD) [47].

The EBSD measurements were performed near the centre (r ~ 0.2 mm) and at the mid-radius position (r ~ 2.5 mm) of the mid-thickness plane of the HPT-processed discs using a TSL-EDAX-Hikari system mounted on a scanning electron microscope (FEG-SEM Zeiss Supra 55 VP) operating at 20 kV.

The equivalent strain, ε_{eq}, imposed during HPT can be calculated from the following equation [48]:

$$\varepsilon_{eq} = \frac{2\pi N r}{\sqrt{3}h} \quad (1)$$

where r is the radial distance from the centre of the disc and h is the thickness of the disc after HPT. Accordingly, Table 1 summarizes the values of ε_{eq} in each HPT-processed disc.

Table 1. Values of the imposed equivalent strain ε_{eq} in different positions (near centre and mid-radius) of HPT-processed discs.

N	***r* (mm)**	**ε_{eq}**
1/2	0.2	0.6
	2.5	7.2
5	0.2	5.7
	2.5	71.9
10	0.2	11.5
	2.5	143.7
20	0.2	23.0
	2.5	287.5

The scanned areas for the AZ31 discs were 40 × 40 μm^2 with a step size of 0.1 μm for N = 0, 1/2, 5 and 10 turns and for the AZ31 disc processed for N = 20 turns the scanned area was 5 × 5 μm^2 with a step size of 20 nm. The scanned area for the initial state (N = 0) of the Mg-0.6Gd alloy was 700 × 2500 μm^2 with a step size of 1 μm, whereas the scanned areas for the HPT-processed Mg-0.6Gd discs (N = 1/2, 5, 10 and 20 turns) were 40 × 40 μm^2 with a step size of 50 nm. The EBSD data were analysed by the Orientation Imaging Microscopy OIM^{TM} software.

The dynamically recrystallized grains were identified using the grain orientation spread (GOS) approach implemented in the OIM™ software, where grains with GOS < 2° are considered fully recrystallized [49].

The texture was analysed using toolbox MTEX by calculating the orientation distribution function (ODF) using the harmonic method (L = 22) and a Gaussian function with a half-width of 5° to model each orientation [50].

Detailed microstructural observations at the mid-radius positions of discs processed for N = 5 turns were performed using a CS-corrected dedicated Thermo Fisher Scientific Spectra scanning transmission electron microscope (STEM) operating at an accelerating voltage of 200 kV. The STEM observations were carried out in the bright-field (BF) and high-angle annular dark field (HAADF) modes. Structural investigations were combined with advanced energy dispersive X-Ray (EDX) point and mapping analyses. Thin foils for observations were prepared using a Focused Ion Beam (FIB) Hitachi NB-5000 microscope.

The microhardness of the samples was measured using a Vickers microhardness tester (SHIMADZU type HMV-2 tester) with a load of 100 g ($Hv_{0.1}$) and a dwell time of 10 s. At least 5 Hv measurements were recorded to obtain the average value for each sample.

3. Results

Figures 1 and 2 present the evolution of the microstructure of AZ31 and Mg-0.6Gd alloys in terms of an inverse pole figure (SD-IPF) map as a function of equivalent strain: (a) ε_{eq} = 0, (b) ε_{eq} = 0.6, (c) ε_{eq} = 7.2, (d) ε_{eq} = 71.9, (e) ε_{eq} = 143.7 and (f) ε_{eq} = 287.5, respectively. The grain boundaries with high misorientations (θ > 15°) are highlighted by a black line. It should be noted that the SD-IPF map of the HPT-processed AZ31 sample at ε_{eq} = 287.5 (Figure 1f) is presented with a different scale bar. The initial microstructures of the AZ31 and Mg-0.6Gd alloys are different and related directly to the processing history. The microstructure of the as-received AZ31 alloy is characterized by deformed grains with a mean grain size of ~12.5 μm and the presence of twins identified as {10-11} contraction twins.

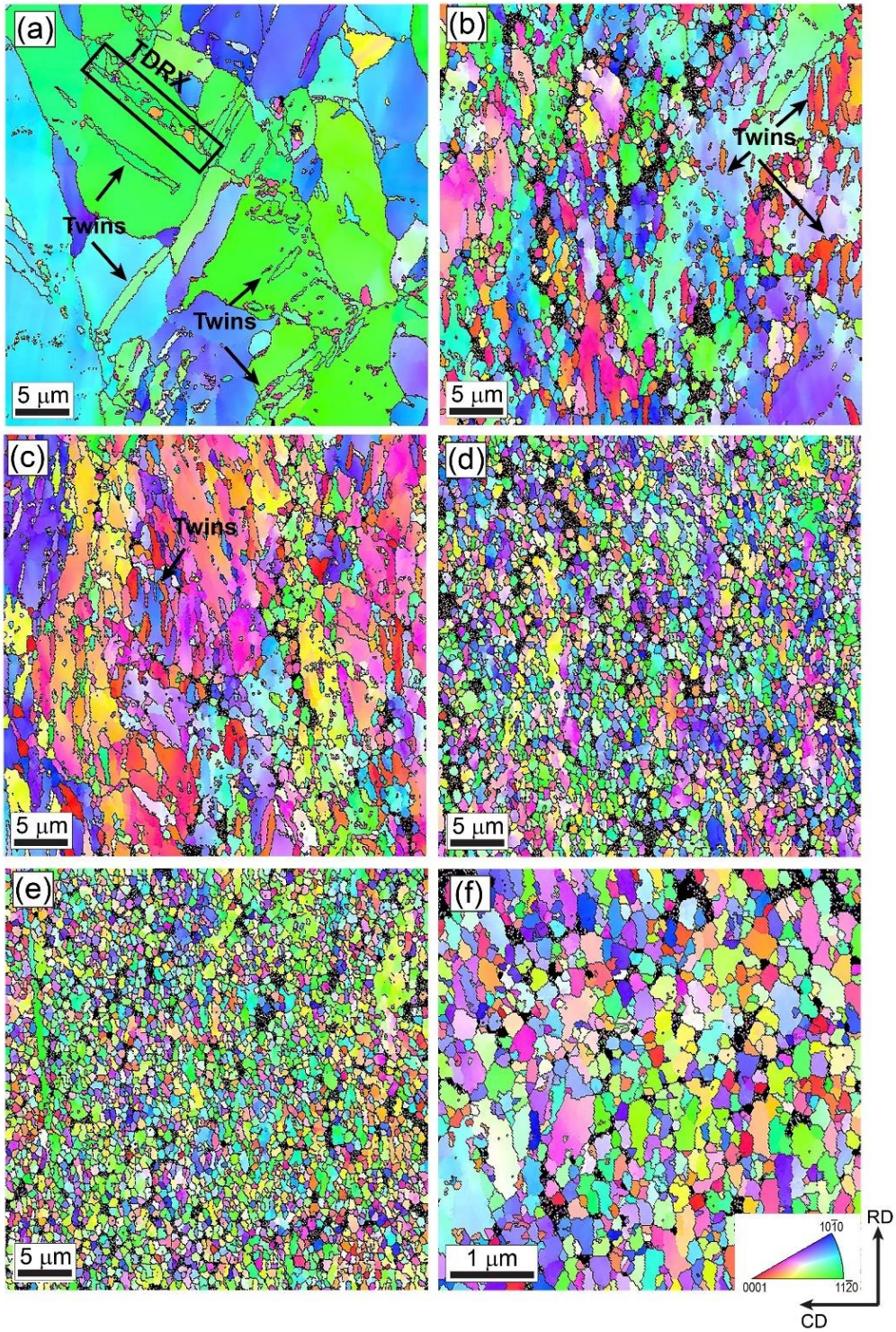

Figure 1: SD-IPF maps of AZ31 alloy HPT processed for (a) ε_{eq} = 0 (initial state), (b) ε_{eq} = 0.6 (centre of N = 1/2 turn), (c) ε_{eq} = 7.2 (middle of N = 1/2 turn), (d) ε_{eq} = 71.9 (middle of N = 5 turns), (e) ε_{eq} = 143.7 (middle of N = 10 turns) and (f) ε_{eq} = 287.5 (middle of N = 20 turns). Note that Figure 1f is presented with different scale bar.

The rectangular box indicates the occurrence of the twin-induced dynamic recrystallization (TDRX) mechanism which is characterized by the formation of recrystallized grains inside the twins [51]. By contrast, the microstructure of the as-received Mg-0.6Gd alloy contains coarse grains with a mean grain size of about ~670 µm which is typical of an as-cast condition.

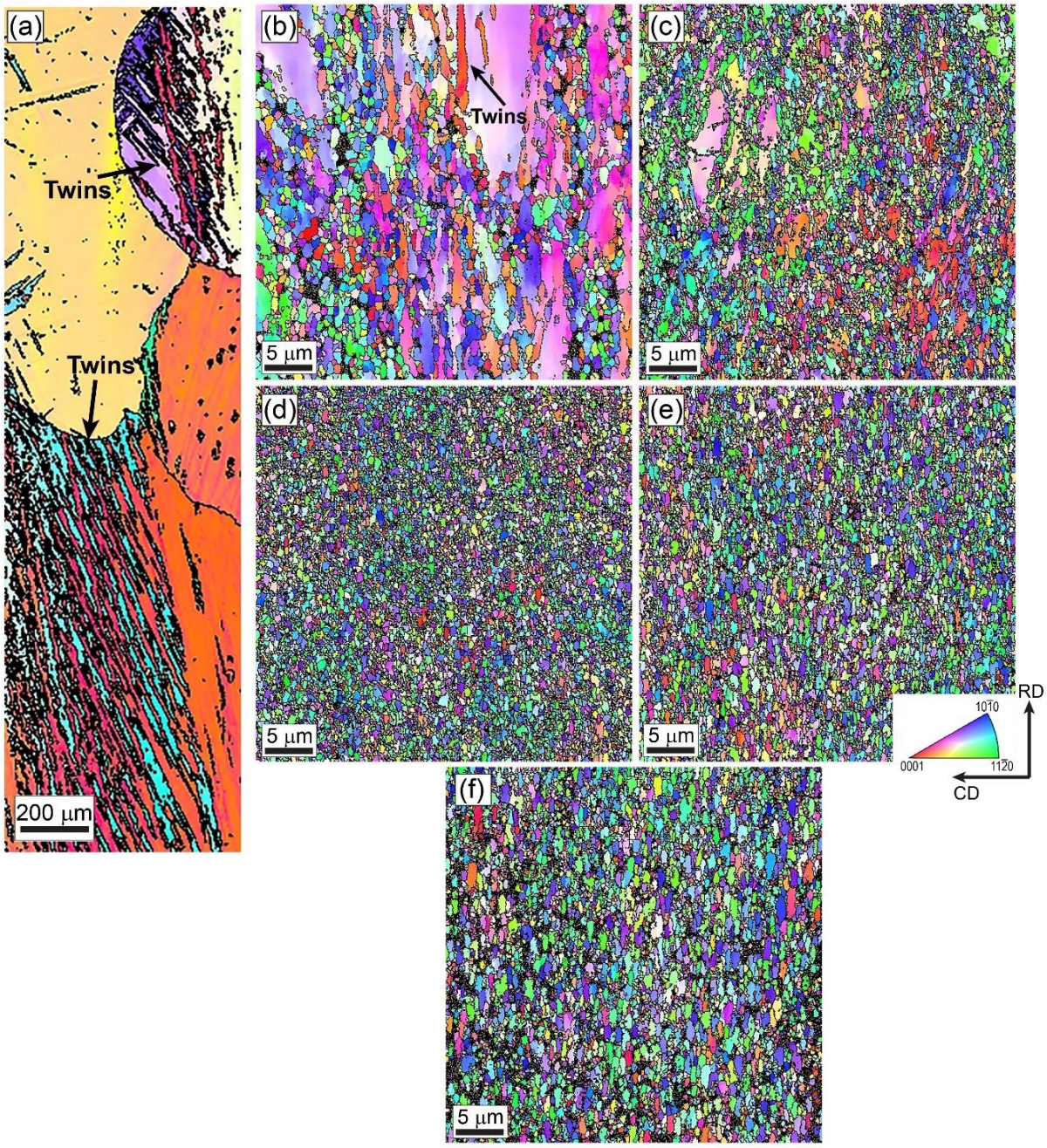

Figure 2: SD-IPF maps of Mg-0.6Gd alloy HPT processed for (a) ε_{eq} = 0 (initial state), (b) ε_{eq} = 0.6 (centre of N = 1/2 turn), (c) ε_{eq} = 7.2 (middle of N = 1/2 turn), (d) ε_{eq} = 71.9 (middle of N = 5 turns), (e) ε_{eq} = 143.7 (middle of N = 10 turns) and (f) ε_{eq} = 287.5 (middle of N = 20 turns).

The microstructure of the as-cast Mg-0.6Gd alloy contains also massive twins identified as {10-12} extension twins in the form of steps and it is reasonable to assume that their presence is due to the mechanical preparation of the sample. The SD-IPF maps indicate that the twins remain present during HPT processing and they are more visible in the AZ31 alloy through strains from 0.6 to 7.2 as shown by the black arrows. However, the fraction of twins decreases with increasing equivalent strain due to the grain refinement. Indeed, the deformation microstructure of both alloys transformed gradually to equiaxed fine grains with increasing equivalent strain. It is interesting to note that the deformation microstructure of the Mg-0.6Gd alloy became more homogeneously distributed (at ε_{eq} = 7.2) than for the AZ31 alloy (at ε_{eq} = 143.7). The evolutions of mean grain size, DRX fraction and HAGBs fraction as a function of equivalent strain in the AZ31 and Mg-0.6Gd alloys are shown in Figure 3.

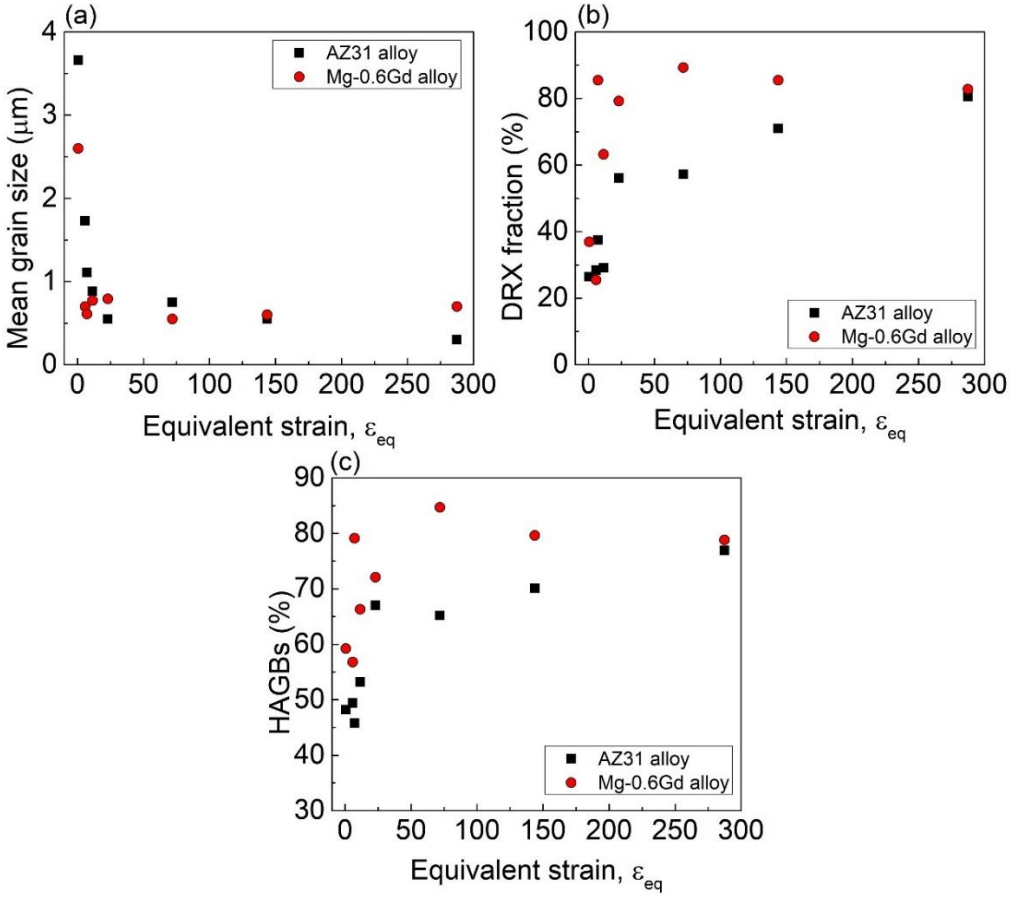

Figure 3: Evolution of (a) mean grain size, (b) DRX fraction, and (c) HAGBs fraction in AZ31 and Mg-0.6Gd alloy as a function of equivalent strain.

The HPT processing at a strain of 0.6 causes a decrease in grain size to 3.6 μm for the AZ31 alloy. Thereafter, the mean grain size of the HPT-processed AZ31 alloy decreases

gradually with increasing equivalent strain to 0.55 μm at ε_{eq} = 23 and then decreases slowly to 0.3 μm at ε_{eq} = 287.5. The mean grain size of the Mg-0.6Gd alloy rapidly deceases from 670 to 2.6 μm after a strain of ε_{eq} = 0.6, then to 0.71 μm at ε_{eq} = 5.7 where it appears to reach a saturation value.

It is apparent from Figure 3b that the fraction of DRX in the Mg-0.6Gd alloy is higher than in the AZ31 alloy. The fraction of DRX was relatively similar in both alloys during low straining (ε_{eq} = 0.6–5.7) but DRX occurred rapidly in the Mg-0.6Gd alloy and reached a high value of 85 % at a strain of ε_{eq} = 7.2 which was a saturated condition. For the AZ31 alloy, the DRX fraction increased slowly but continuously with increasing strain and the microstructure became essentially fully recrystallized (about 80 %) at a strain ε_{eq} = 287.5. Consequently, the fraction of HAGBs increases with increasing equivalent strain for both alloys, as demonstrated in Figure 3c. However, it is obvious that the fraction of HAGBs is higher in the Mg-0.6Gd alloy than in the AZ31 alloy, especially during an equivalent strain range of ε_{eq} = 5.4–143.7.

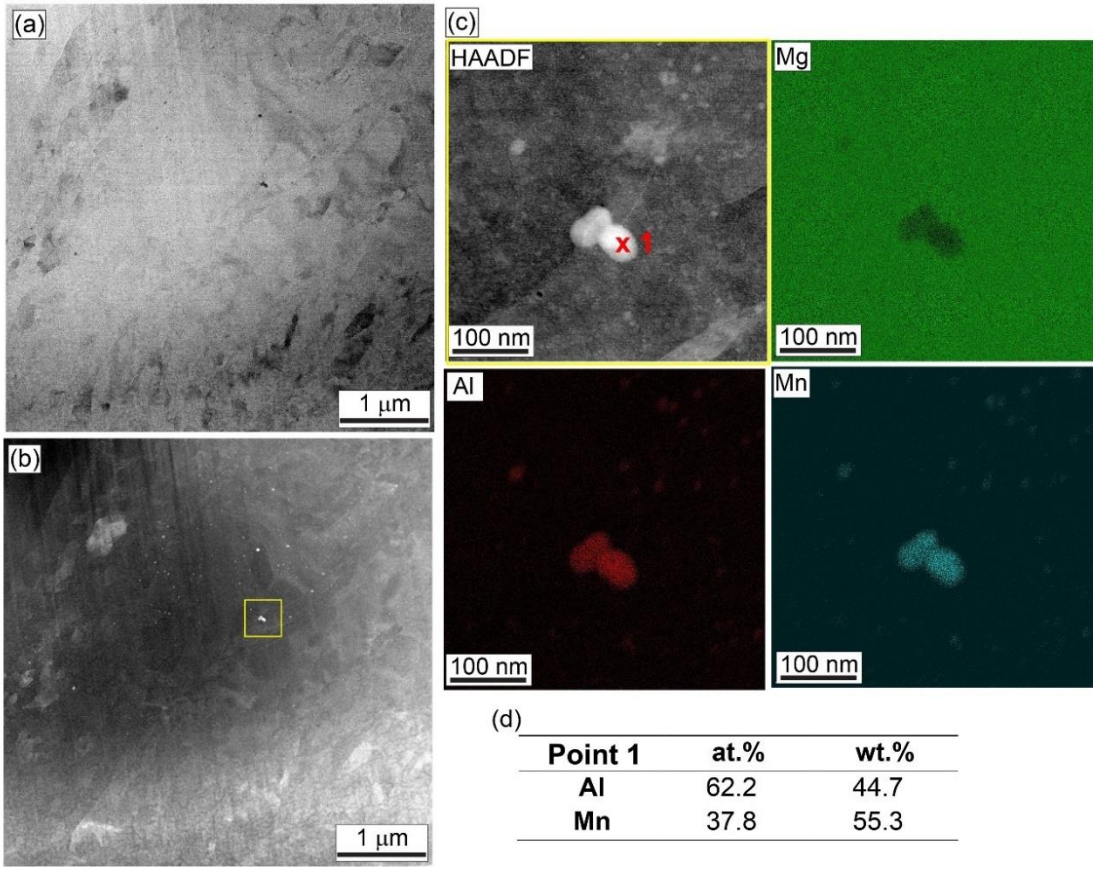

(d)

Point 1	at.%	wt.%
Al	62.2	44.7
Mn	37.8	55.3

Figure 4: STEM images in (a) BF and (b) HAADF at low magnification near the mid-radius of the AZ31 disc processed for N = 5 turns (ε_{eq} = 71.9), and (c) high magnification of yellow box showing the EDS mapping for Mg, Al and Mn elements and EDS analysis of particles present at point 1.

Figures 4 and 5 show STEM images in (a) BF and (b) HAADF at low magnification after processing for N = 5 turns (ε_{eq} = 71.9) near the mid-radius of the AZ31 and Mg-0.6Gd disc, respectively. In addition, Figure 4c shows a high magnification of the yellow box of the HPT-processed AZ31 alloy showing the EDS mapping for the Mg, Al, and Mn elements and the EDS analysis of particles present at point 1.

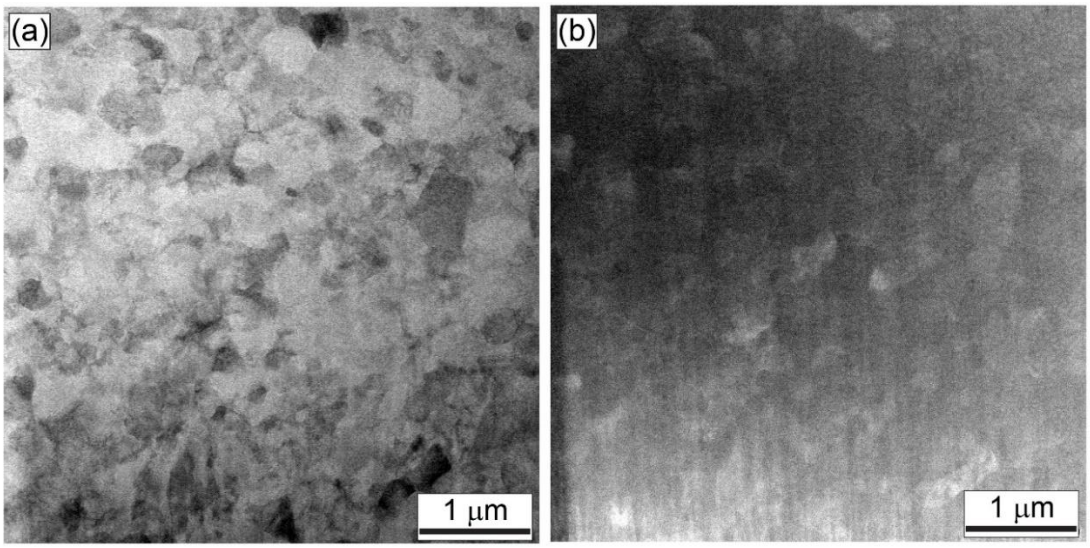

Figure 5: STEM images in (a) BF and (b) HAADF at low magnification near the mid-radius of the Mg-0.6Gd disc processed for N = 5 turns (ε_{eq} = 71.9).

Observations by STEM confirmed extensive grain refinement in both alloys although, the images (BF mode) indicate that the AZ31 alloy exhibits a more homogeneous microstructure in terms of grain refinement when compared with the Mg-0.6Gd alloy (Figures 4a and 5a). The grain size calculated for the AZ31 and Mg-0.6Gd alloys was 260 ± 30 nm and 650 ± 68 nm, respectively. The HAADF images (Figures 4b and 5b) demonstrate a net difference in the presence of second phase particles. No particles are visible in the HAADF images of the Mg-0.6Gd sample indicating the fragmentation and dissolution of the metastable Mg_5Gd particles which were present in the as-cast state, where this is consistent with an earlier report [37]. High magnification observations of the AZ31 sample showed a high concentration of small spherical nanoparticles having sizes from 10-45 nm. The EDS analysis (Fig. 4c) indicates that these particles consist mainly of Al and Mn and the atomic and weight percentages shown in Figure 4d demonstrate that these Mn-containing particles are stable Al_8Mn_5 [52]. It must be noted that the fraction of the Mg element (present only in the matrix) was excluded in order to show Al/Mn proportions.

Figures 6 and 7 show the recalculated {0002} pole figures and ODF sections at φ_2 = 0 and 30° of the HPT processed AZ31 and Mg-0.6Gd alloys for (a) ε = 0, (b) ε = 0.6, (c) ε = 7.2, (d) ε = 71.9, (e) ε = 143.7, and (f) ε = 287.5, respectively. The ideal shear texture component positions on the RD-CD plane for materials with HCP structure [47] are also present in both figures (Figures 6g and 7g) and their description in the form of the Euler angles (φ_1, Φ, φ_2) is given in Table 2. The initial texture of the AZ31 alloy shows the presence of a basal texture (B-fiber) which is a typical texture formed during the rolling of Mg-based alloys [53, 54].

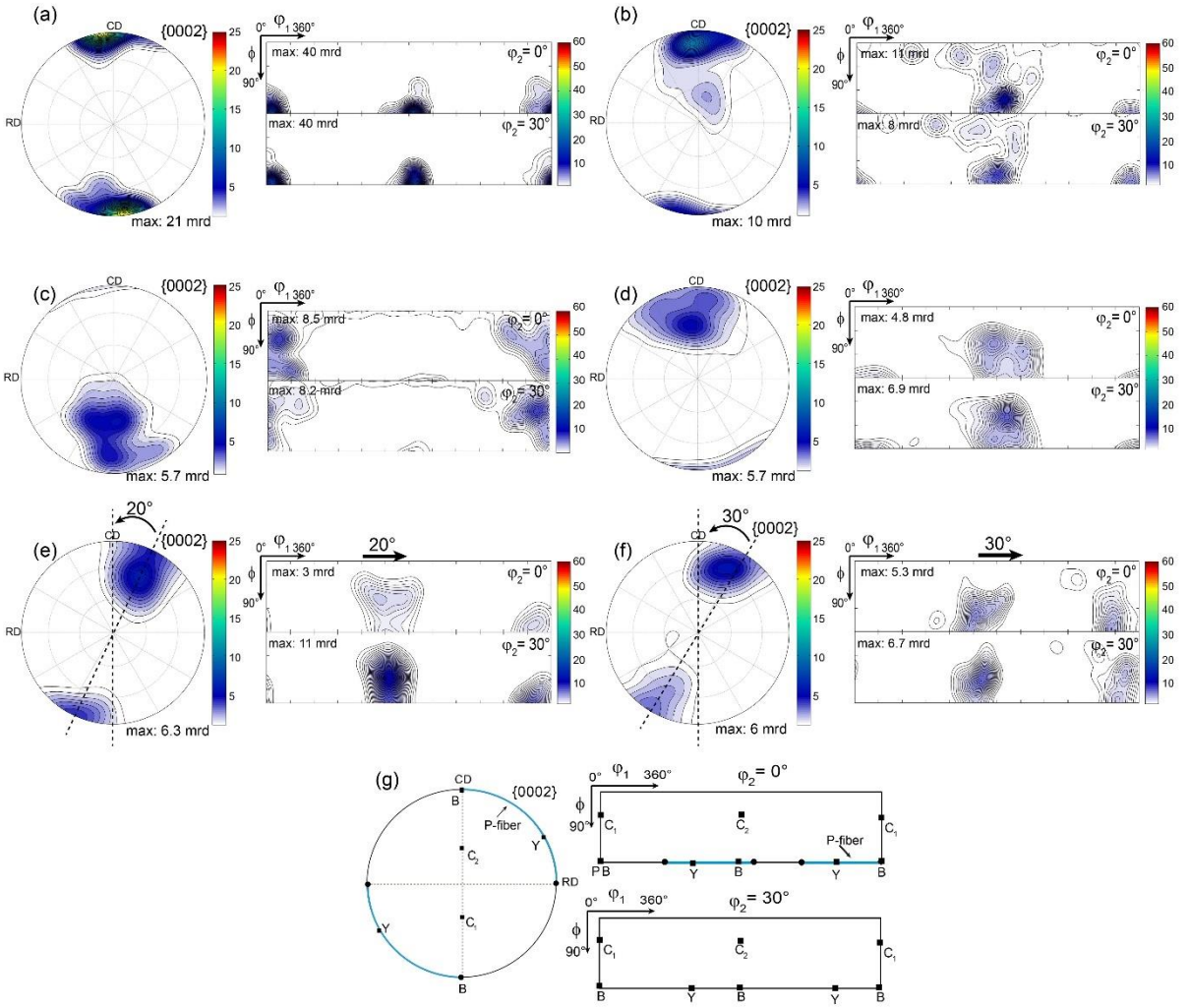

Figure 6: Recalculated {0002} pole figures and ODF sections at φ_2 = 0 and 30° of AZ31 alloy HPT processed for (a) ε_{eq} = 0 (initial state), (b) ε_{eq} = 0.6 (centre of N = 1/2 turn), (c) ε_{eq} = 7.2 (middle of N = 1/2 turn), (d) ε_{eq} = 71.9 (middle of N = 5 turns), (e) ε_{eq} = 143.7 (middle of N = 10 turns), (f) ε_{eq} = 287.5 (middle of N = 20 turns) and (g) the ideal shear texture components positions on CD-RD plane for materials with HCP structure [47].

Table 2. Position of ideal shear texture components for HCP materials and alloys projected in the CD-RD plane [47].

Notation	B-fiber	P-fiber	Y-fiber	C_1-fiber	C_2-fiber
(φ_1, Φ, φ_2)	(360, 90, 0-60)	(90-180, 90, 0)	(300, 90, 0-60)	(0, 30, 0-60)	(180, 30, 0-60)

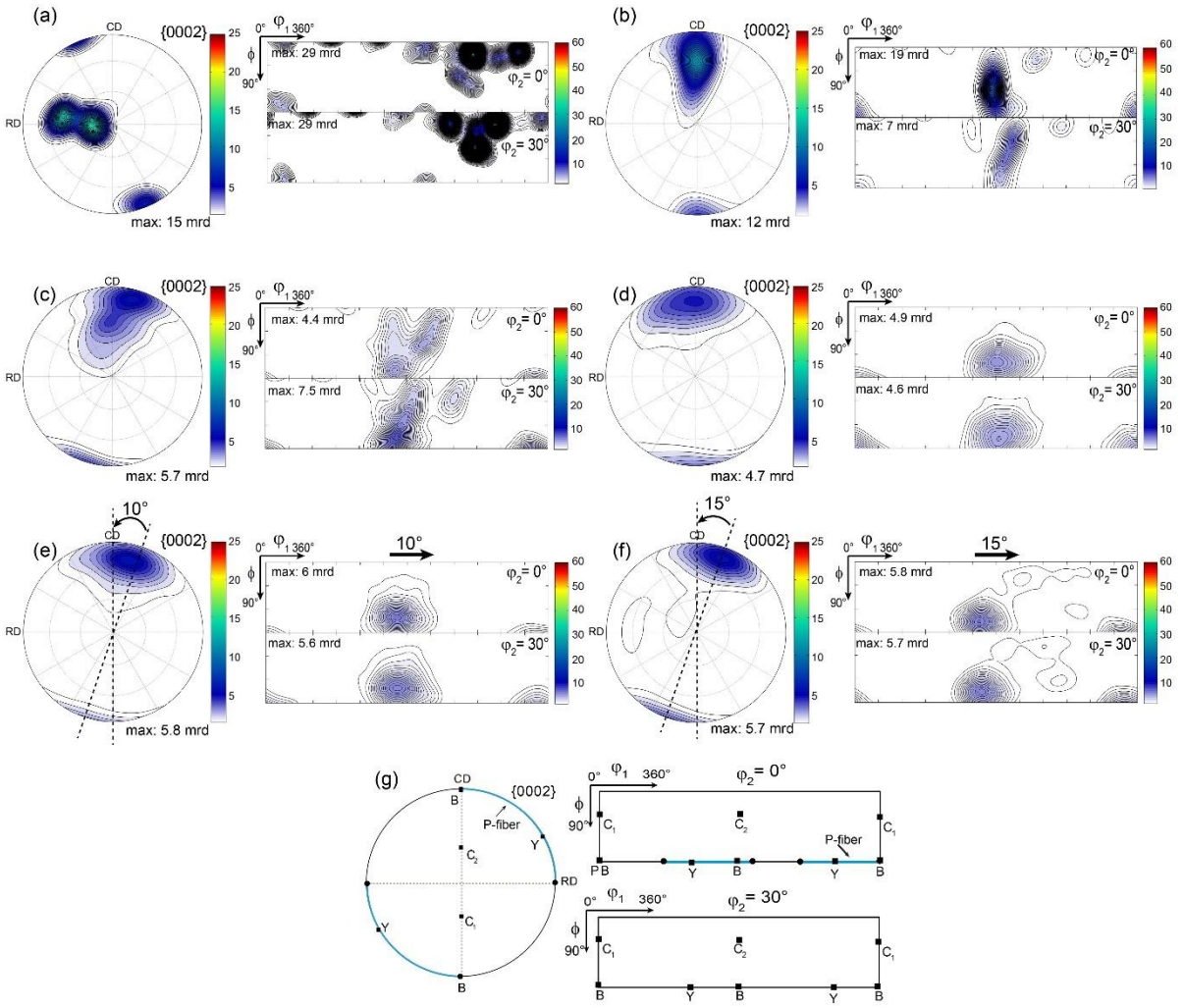

Figure 7: Recalculated {0002} pole figures and ODF sections at φ_2 = 0 and 30° of Mg-0.6Gd alloy HPT processed for (a) ε_{eq} = 0 (initial state), (b) ε_{eq} = 0.6 (centre of N = 1/2 turn), (c) ε_{eq} = 7.2 (middle of N = 1/2 turn), (d) ε_{eq} = 71.9 (middle of N = 5 turns), (e) ε_{eq} = 143.7 (middle of N = 10 turns), (f) ε_{eq} = 287.5 (middle of N = 20 turns) and (g) the ideal shear texture components positions on CD-RD plane for materials with HCP structure [47].

The HPT processing at a strain of 0.6 (Figure 6b) led to the development of the C_2-fiber. As can be seen from Figure 6c, the C_1-fiber is developed with a weak B-fiber at a strain of 7.2. Again, the C_2 and basal fibers appeared at a strain of 71.9 with significant deviation from their ideal positions as can be observed with further increasing strain at ε_{eq} =143.7 (about 20° towards

RD) and 287.5 (about 30° towards RD). It is evident from the {0002} pole figure (Figure 6f) that there is the presence of a deviated C_1-fiber at a strain of 287.5.

The identification of texture type (see Figure 7a) of the as-cast Mg-0.6Gd sample was not possible since the sample exhibits limited grain numbers as revealed in Figure 2a. However, the B-fiber and C_2-fiber formed rapidly after HPT processing at ε_{eq} = 0.6. The C_2-fiber disappears with increasing strain at ε = 71.9 leading to a dominant basal texture through the entire strain. It can be noticed that there is a small deviation of basal fiber from its ideal position with increasing strain from ε_{eq} = 143.7 (about 10° towards RD) to ε_{eq} = 287.5 (about 15° towards RD).

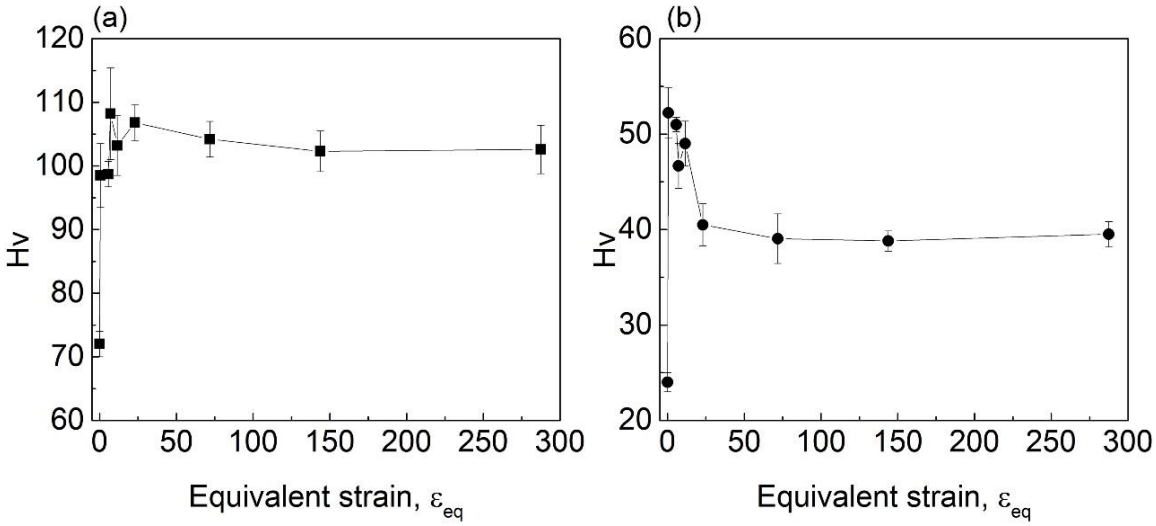

Figure 8: Evolution of microhardness as a function of equivalent strain of: (a) AZ31, and (b) Mg-0.6Gd alloys.

Figures 8a and b present the evolution of microhardness as a function of the equivalent strain for the AZ31 and Mg-0.6Gd alloys, respectively. The microhardness of the initial states of the AZ31 and Mg-0.6Gd alloys were 72 and 24 Hv, respectively. The microhardness of the AZ31 alloy increased with increasing strain to reach a value of 108 Hv at a strain of ε_{eq} = 7.2 and slightly decreased to reach a saturated value of 102.6 Hv. In the case of the Mg-0.6Gd alloy, the microhardness goes through three stages. First, the microhardness increases with increasing equivalent strain to a maximum value of 53.1Hv at ε_{eq} = 3.6. Second, it decreases with increasing strain to 39.5 Hv at ε_{eq} = 71.9, and then finally it statures at this value up to a strain of ε_{eq} = 287.5.

4. Discussion

The evolution of the microstructural parameters, such as mean grain size, DRX and HAGBs fractions in the AZ31 and Mg-0.6Gd alloys through HPT processing shown in Figures 1–3 demonstrate that the grain refinement of both alloys is obtained by the CDRX process. Nevertheless, the DRX kinetics and consequently the grain refinement behavior were different between the two alloys. In general, the grain refinement of both alloys can be separated into two stages. For the AZ31 alloy, stage I occurred during ε_{eq} = 0.6-11.5 where the DRX and HAGBs fractions increase and the mean grain size decreases gradually from 25 to 1.1 µm and in stage II (ε_{eq} = 11.5-287.5) the DRX and HAGBs fractions continue to increase and the grain size decreases slowly by comparison with stage I to reach a value of 0.3 µm at a strain of 287.5. For the Mg-0.6Gd alloy, the DRX and HAGBs fractions increase quickly during stage I (ε_{eq} = 0.6-5.7) leading to the formation of an equiaxed microstructure with a mean grain size of 0.7 µm and then stage II (ε_{eq} = 5.7-287.5) shows the saturations of the mean grain size and the HAGBs and DRX fractions. Such behavior is consistent with the evolution of microhardness shown in Figure 8. The evolution of microhardness of the AZ31 alloy indicated a strain hardening without recovery [55, 56], while that of the Mg-0.6Gd alloy shows a strain hardening with recovery and dynamic recrystallization [55, 56].

It must be noted that the present results show that the AZ31 and Mg-0.6Gd alloys exhibit an inverse behavior compared with that reported for the AZ31 and Mg-1.5Gd alloys under conventional processing [41]. The enhancement of DRX is mainly attributed to the stored energy during deformation processing. At RT and low strains, the deformation of Mg-based alloys is accommodated by twinning and dislocations generated mainly from the activation of <a> basal slip. Hence, to further analyze the DRX behavior, the presence of twins and an estimate of the dislocation densities at a low strain, ε_{eq} = 0.6, are compared for both alloys as in Figures 9 and 10.

Figures 9a and 9b present the Image Quality (IQ) maps highlighted by the common twinning mode found in Mg-based alloy: {10-11}-contraction twinning (56°<11-20>) and {10-12}-extension twinning (86°<11-20>). The {10-11}-contraction and {10-12}-extension twins are identified with an error angle of 10° and labeled by blue and green colors, respectively. The fractions of twins are shown in the upper IQ maps (Figures 9a and 9b) and seem similar in both samples except that there is a higher fraction of {10-12}-extension twin in the AZ31 alloy (11.8 % vs. 8.0%). The magnification of the yellow box shown in Figures 9c and g demonstrates that the twins have different shapes depending on the alloy. Figure 9c shows that the extension twins in the AZ31 alloy have lenticular shape structures. It is interesting to note that the extension

twins are responsible for the development of the C_2-fiber as indicated by the SD-IPF map and the corresponding {0002} pole figure (Figures 9d and 9f).

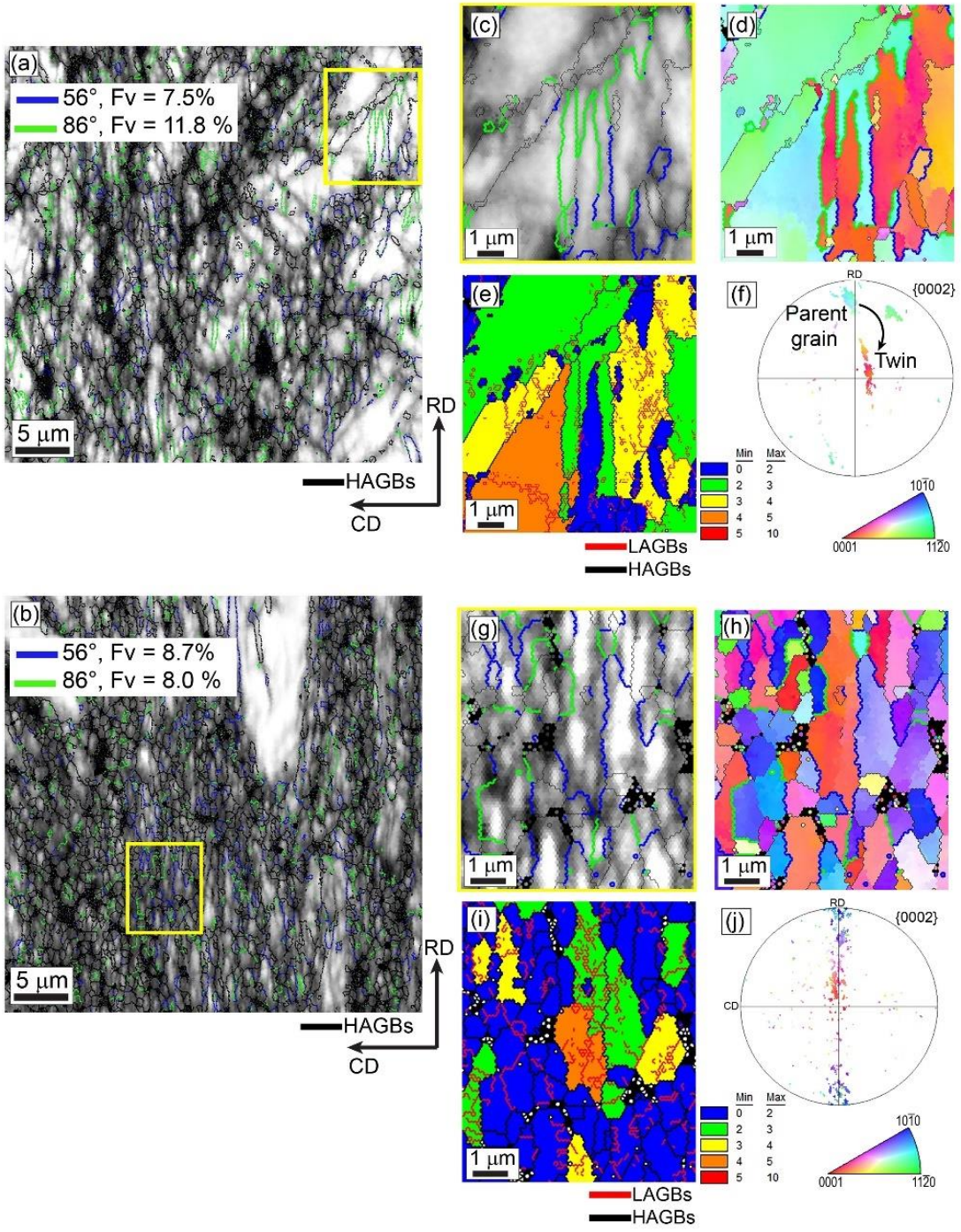

Figure 9: (a, b) Image Quality (IQ) map highlighted by contraction twin (blue color) and extension twin (green color) in HPT-processed AZ31 and Mg-0.6Gd alloys at ε_{eq} = 0.6, respectively. (c, d, e, f) and (g, h, i, j) IQ, SD-IPF, GOS maps and {0002} corresponding pole figure of yellow box of HPT-processed AZ31 and Mg-0.6Gd samples, respectively.

By contrast, Figures 9g and 9i show that the extension and contraction twins present in the Mg-0.6Gd alloy are mostly boundaries for the dynamically recrystallized grains. The SD-IPF map and the corresponding {0002} pole figure shown in Figures 9h and 9j confirm that the development of the C_2-fiber comes from the activation of contraction and extension twins.

Despite the fact that the AZ31 and Mg-0.6Gd alloys exhibit different initial textures (Figures 6a and 7a), similar textures composed of basal and C_2-fiber formed in both alloys at a low strain (ε_{eq} = 0.6). In fact, most hexagonal materials develop the B-fiber during HPT processing and exactly during the compression stage [47, 57] due to the easy activation of the <a>-basal slip system which orients the basal planes parallel to the shear plane producing a typical basal texture [47, 58]. It is well known that twinning has more effect on texture modification than grain refinement due to the creation of a high misorientation angle between twins and their parent grains [24]. It is also worth noting that the development of the C_1-fiber in the HPT-processed AZ31 sample at ε_{eq} = 7.2 (Figure 6c) is due to the activation of twins as can be seen from Figure 1c. The C_1 and C_2 fibers are considered as pairs since they are defined as *c*-fiber where the *c*-axis is first rotated 90° in the shear direction, then ±30° in the shear plane direction [58].

The evolutions of texture show that the C_1 and C_2 fibers remain present in the AZ31 alloy (Figure 6) but with a significant deviation from their ideal position with increasing strain. First, the lenticular extension twins can propagate and grow rapidly with further strain due to their high mobility [59] and eventually consume the parent grain which can explain the persistence of the C_1 and C_2 fibers. Second, the deviation of the texture at higher stains is attributed to the torsional straining imposed by the rotation of the anvil during HPT processing [47]. However, the C_2-fiber completely disappeared in the Mg-0.6Gd alloy (Figure 7) with increasing strain and this indicates that the effect of twins on the texture evolution of the Mg-0.6Gd alloy is not permanent. In practice, the twin boundaries can strongly block the dislocation motion which contributes to their accumulation and the formation of LAGBs [60]. As can be seen in Figures 9e and 9i, the GOS maps indicate that within the contraction twins and near the twin boundaries there are LAGBs which will transform into HAGBs and eventually into newly refined grains with further strain. These new grains may have similar orientations to the twin [24, 61] or they may develop different orientations [62]. Unlike the extension twins, contraction twins have a very low mobility [63] so that the recrystallized grains within them will not grow and hence they will be devoured by the neighboring grains with further strain.

To estimate the dislocation density, ρ, especially the geometrically necessary dislocations, a Kernel Average Misorientation (KAM) method was applied following the expression [64]:

$$\rho = \frac{\theta_{KAM}}{db} \quad (2)$$

where b is the Burgers vector, d is the scan step size and θ_{KAM} is the average misorientation angle.

It should be mentioned that the accurate dislocation density depends strongly on choice of various EBSD parameters like the size of the kernel, the EBSD step size and the threshold angle. Since the absolute dislocation density values were not pursued in this investigation, the θ_{KAM} was calculated from the mean misorientation angle between the point and its 3rd neighbors and by excluding misorientations of $\theta > 5°$. These chosen parameters are compatible with the average grain size even for the highest strains (about 0.3 µm in the case of AZ31 alloy).

Figures 10a and b present the KAM maps at $\varepsilon_{eq} = 0.6$ for the HPT-processed AZ31 and Mg-0.6Gd alloys, respectively. The θ_{KAM} and ρ values are shown in the upper KAM maps. The results indicate that the AZ31 alloy ($\rho = 8.3 \times 10^{14}$ m^{-2}) stored more energy than the Mg-0.6Gd alloy ($\rho = 7.1 \times 10^{14}$ m^{-2}). The evolution of dislocation density as a function of equivalent strain for both alloys is presented in Figure 10c. As can be seen, the dislocation density of the AZ31 alloy increases with increasing strain at 11.5 and then starts to decrease indicating the occurrence of DRX and the formation of new grains. By contrast, the dislocation density of the Mg-0.6Gd alloy is stable around 7×10^{14} m^{-2} through the entire strain which demonstrates that an equilibrium is reached between the generation of dislocations and the formation of new grains. This may explain the saturation of the grain refinement at 0.7 µm with increasing strain (ε_{eq} = 5.7-287.5). In this case, the new dislocations prevent the HAGBs of the dynamically recrystallized grains from migration and thereby they limit the grain growth. It is known that a high stored energy will increase the rate of recrystallization [26]. Figure 10 shows that the stored energy is higher in the AZ31 alloy but the DRX was restricted by comparison with the Mg-0.6Gd alloy which shows a lower stored energy and a fast DRX.

The presence of nano-size particles of Al_8Mn_5 (shown in Figure 4) may be one of the reasons for the retardation of DRX in the AZ31 alloy. On the one hand, it is recognized that the pinning effect of large second particles (> 1µm) on the dislocation motion will increase the stored energy around them and promote DRX via the particle-stimulated nucleation mechanism [26, 65]. The morphology, size, quantity and distribution of second particles are important parameters affecting the DRX process [26, 60, 66, 67]. On the other hand, it was found that

DRX is restricted when the small second phase particles pinned the dislocations and sub-grain boundaries resulting from the DRX process and inhibited their transformation to HAGBs [60, 67] which is mostly the case in the present AZ31 alloy. The second reason to consider for the DRX kinetics is the nature and concentration of the alloying element. It is expected that the effect of 3 % Al and 1 % Zn in the AZ31 alloy on segregation to grain boundaries and the limitation of their mobility in solute drag will be greater than the low concentration of 0.6 % Gd in the Mg-0.6Gd alloy.

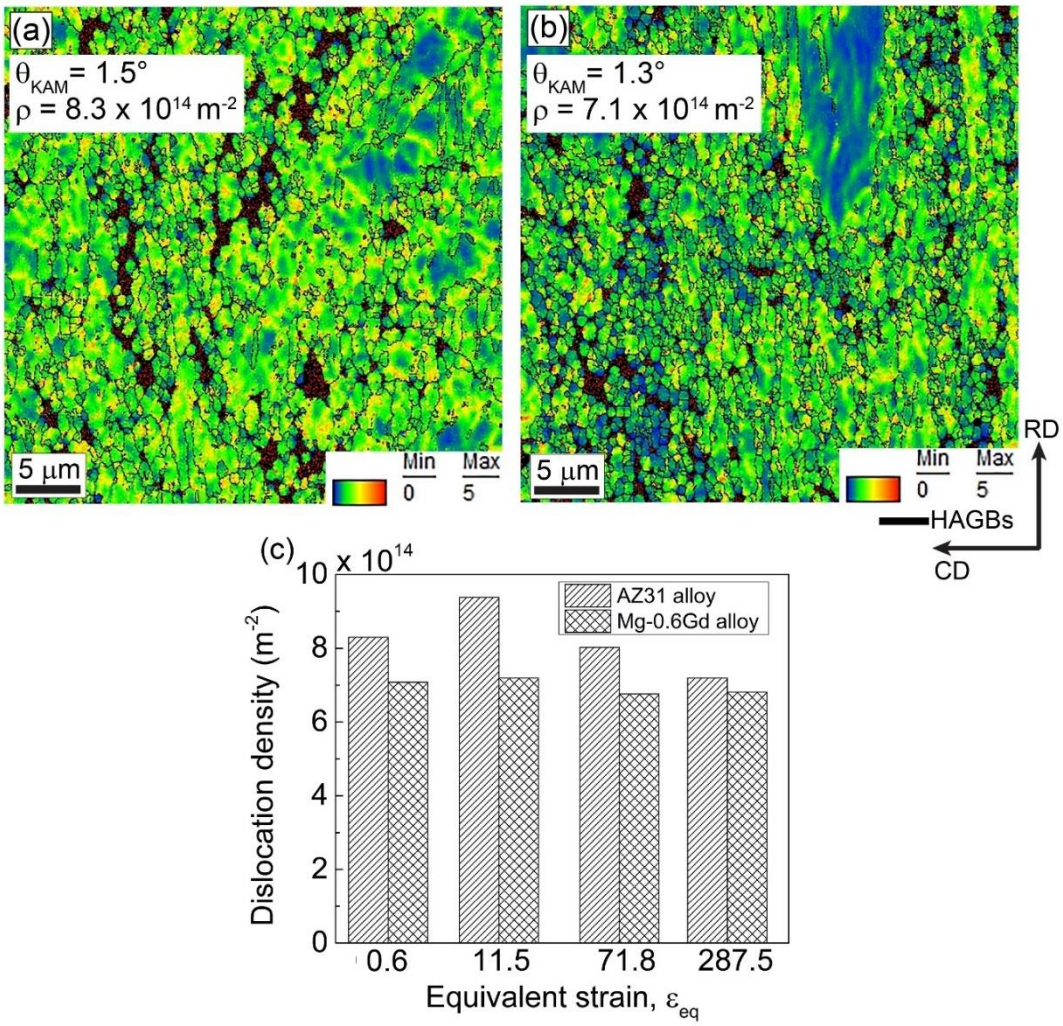

Figure 10: KAM map of (a) AZ31, (b) Mg-0.6Gd alloys HPT processed at ε_{eq} = 0.6 and c) evolution of dislocation density as a function of equivalent strain for both alloys.

The difference in the initial microstructure is also another reason for the difference in the DRX kinetics. As shown in Figures 1a and 2a, the AZ31 alloy contains more grain boundaries than the Mg-0.6Gd alloy and these eventually act as pinning points delaying further dislocation propagation [68] and causing grain boundary strengthening for the AZ31 alloy. The

latter proposal is supported by the high dislocation density shown in Figure 10c and the evolution of the microhardness presented in Figure 8.

The present results demonstrate that HPT processing has the ability to change the deformation behavior and the DRX kinetics of Mg-based alloys by comparison with conventional thermomechanical processing. This suggests that in future it will be interesting to compare the static recrystallization of HPT-processed AZ31 and Mg-0.6Gd alloys.

5. Summary and conclusions

Alloys of AZ31 and Mg-0.6Gd were processed by HPT at RT through ε_{eq} = 0.6–287.5 and their microstructure, texture and microhardness evolutions were reported and compared. The main findings can be summarized as follows:

- The EBSD, STEM and microhardness results show that the grain refinement of each alloy was different and it was the opposite of that generally reported under conventional deformation.
- The AZ31 alloy exhibits a gradual and continuous formation of ultrafine grains with a mean grain size of ~0.3 μm through the entire strain due to the retardation of DRX. By contrast, DRX was fast in the Mg-0.6Gd alloy leading to a rapid ultrafine grain microstructure over a strain range of ε_{eq} = 0.6-5.7 with a mean grain size of ~0.7 μm and remaining stable at a strain range of ε_{eq} = 5.7-287.5.
- The restriction of DRX in the AZ31 alloy was explained by the presence of stable Al_8Mn_5 particles, solute drag and grain boundary strengthening.
- The evolution of microhardness in the AZ31 alloy showed a strain hardening without recovery whereas the Mg-0.6Gd alloy displayed a strain hardening with recovery.
- The AZ31 alloy was characterized by the development of deviated B, C_1, and C_2 fibers. By contrast, the Mg-0.6Gd alloy exhibited a relatively stable B-fiber. The formation and disappearance of C_1 and C_2 fibers was due to the activation and evolution of mechanical twinning.

Acknowledgements

Dr-Ing. N. Hort and Dr. D. Letzig (MagIC, Germany) and Dr-Ing. Talal Al-Samman (RWTH-Aachen University, Germany) are gratefully acknowledged for providing the AZ31 and Mg-0.6Gd alloys, respectively. Two of the authors were supported by the European Research Council under Grant Agreement No. 267464-SPDMETALS (YH and TGL).

Data Availability: The raw/processed data required to reproduce these findings cannot be shared at this time as the data also forms part of an ongoing study.

References

[1] R. Radha, D. Sreekanth, Insight of magnesium alloys and composites for orthopedic implant applications – a review, Journal of Magnesium and Alloys 5(3) (2017) 286-312.
[2] J. Song, J. She, D. Chen, F. Pan, Latest research advances on magnesium and magnesium alloys worldwide, Journal of Magnesium and Alloys 8(1) (2020) 1-41.
[3] G. Wu, C. Wang, M. Sun, W. Ding, Recent developments and applications on high-performance cast magnesium rare-earth alloys, Journal of Magnesium and Alloys 9(1) (2021) 1-20.
[4] M.P. Medeiros, D.R. Lopes, M. Kawasaki, T.G. Langdon, R.B. Figueiredo, An Overview on the Effect of Severe Plastic Deformation on the Performance of Magnesium for Biomedical Applications, Materials, 2023.
[5] M.H. Yoo, Slip, twinning, and fracture in hexagonal close-packed metals, Metallurgical Transactions A 12(3) (1981) 409-418.
[6] G. Han, H.-K. Park, H.-K. Kim, T.-S. Jun, Local and global deformation behaviour in rolled pure magnesium sheets at room temperature under different strain rates, Materials Science and Engineering: A 762 (2019) 138110.
[7] J. Wu, L. Jin, J. Dong, F. Wang, S. Dong, The texture and its optimization in magnesium alloy, Journal of Materials Science & Technology 42 (2020) 175-189.
[8] R.E. Reed-Hill, W.D. Robertson, Deformation of magnesium single crystals by nonbasal slip, JOM 9(4) (1957) 496-502.
[9] Z. Wu, R. Ahmad, B. Yin, S. Sandlöbes, W.A. Curtin, Mechanistic origin and prediction of enhanced ductility in magnesium alloys, Science (New York, N.Y.) 359(6374) (2018) 447-452.
[10] A. Chapuis, J.H. Driver, Temperature dependency of slip and twinning in plane strain compressed magnesium single crystals, Acta Materialia 59(5) (2011) 1986-1994.
[11] J. Hirsch, T. Al-Samman, Superior light metals by texture engineering: Optimized aluminum and magnesium alloys for automotive applications, Acta Materialia 61(3) (2013) 818-843.
[12] J. Xie, J. Zhang, Z. You, S. Liu, K. Guan, R. Wu, J. Wang, J. Feng, Towards developing Mg alloys with simultaneously improved strength and corrosion resistance via RE alloying, Journal of Magnesium and Alloys 9(1) (2021) 41-56.
[13] E.A. Ball, P.B. Prangnell, Tensile-compressive yield asymmetries in high strength wrought magnesium alloys, Scripta Metallurgica et Materialia 31(2) (1994) 111-116.
[14] K. Hantzsche, J. Bohlen, J. Wendt, K.U. Kainer, S.B. Yi, D. Letzig, Effect of rare earth additions on microstructure and texture development of magnesium alloy sheets, Scripta Materialia 63(7) (2010) 725-730.
[15] T. Al-Samman, X. Li, Sheet texture modification in magnesium-based alloys by selective rare earth alloying, Materials Science and Engineering: A 528(10) (2011) 3809-3822.
[16] A. Imandoust, C.D. Barrett, T. Al-Samman, K.A. Inal, H. El Kadiri, A review on the effect of rare-earth elements on texture evolution during processing of magnesium alloys, Journal of Materials Science 52(1) (2017) 1-29.
[17] R.K. Sabat, A.P. Brahme, R.K. Mishra, K. Inal, S. Suwas, Ductility enhancement in Mg-0.2%Ce alloys, Acta Materialia 161 (2018) 246-257.

[18] M.R. Barnett, Influence of deformation conditions and texture on the high temperature flow stress of magnesium AZ31, Journal of Light Metals 1(3) (2001) 167-177.
[19] T. Al-Samman, G. Gottstein, Dynamic recrystallization during high temperature deformation of magnesium, Materials Science and Engineering: A 490(1) (2008) 411-420.
[20] H. Azzeddine, D. Bradai, Texture and Microstructure of WE54 Alloy after Hot Rolling and Annealing, Materials Science Forum 702-703 (2012) 453-456.
[21] H. Azzeddine, D. Bradai, On the texture and grain growth in hot-deformed and annealed WE54 alloy, International Journal of Materials Research 103(11) (2012) 1351-1360.
[22] S.K. Mishra, S.M. Tiwari, J.T. Carter, A. Tewari, Texture evolution during annealing of AZ31 Mg alloy rolled sheet and its effect on ductility, Materials Science and Engineering: A 599 (2014) 1-8.
[23] D. Elfiad, Y.I. Bourezg, H. Azzeddine, D. Bradai, Investigation of texture, microstructure, and mechanical properties of a magnesium–lanthanum alloy after thermo-mechanical processing, International Journal of Materials Research 107(4) (2016) 315-323.
[24] F. Guerza-Soualah, H. Azzeddine, T. Baudin, A.-L. Helbert, F. Brisset, D. Bradai, Microstructural and textural investigation of an Mg–Dy alloy after hot plane strain compression, Journal of Magnesium and Alloys 8(4) (2020) 1198-1207.
[25] F. Guerza-Soualah, A. Hanna, H. Azzeddine, A.-L. Helbert, F. Brisset, T. Baudin, D. Bradai, The deformation and recrystallization behaviour of an Mg-Dy alloy processed by plane strain compression, Materials Today Communications 24 (2020) 101239.
[26] F.J. Humphreys, M. Hatherly, Recrystallization and related annealing phenomena, second ed., Elsevier, Oxford, 2004.
[27] J. Zhao, Y. Deng, F. Xu, J. Zhang, Effects of Initial Grain Size of Al-Zn-Mg-Cu Alloy on the Recrystallization Behavior and Recrystallization Mechanism in Isothermal Compression, Metals 9(2) (2019) 110.
[28] X.Y. Yang, H. Miura, T. Sakai, Initial Grain Size Effect of Dynamic Recrystallization of Magnesium Alloy AZ31, Materials Science Forum 426-432 (2003) 611-616.
[29] T. Sakai, A. Belyakov, R. Kaibyshev, H. Miura, J.J. Jonas, Dynamic and post-dynamic recrystallization under hot, cold and severe plastic deformation conditions, Progress in Materials Science 60 (2014) 130-207.
[30] A.P. Zhilyaev, T.G. Langdon, Using high-pressure torsion for metal processing: Fundamentals and applications, Progress in Materials Science 53(6) (2008) 893-979.
[31] K. Edalati, A. Bachmaier, V.A. Beloshenko, Y. Beygelzimer, V.D. Blank, W.J. Botta, K. Bryła, J. Čížek, S. Divinski, N.A. Enikeev, Y. Estrin, G. Faraji, R.B. Figueiredo, M. Fuji, T. Furuta, T. Grosdidier, J. Gubicza, A. Hohenwarter, Z. Horita, J. Huot, Y. Ikoma, M. Janeček, M. Kawasaki, P. Král, S. Kuramoto, T.G. Langdon, D.R. Leiva, V.I. Levitas, A. Mazilkin, M. Mito, H. Miyamoto, T. Nishizaki, R. Pippan, V.V. Popov, E.N. Popova, G. Purcek, O. Renk, Á. Révész, X. Sauvage, V. Sklenicka, W. Skrotzki, B.B. Straumal, S. Suwas, L.S. Toth, N. Tsuji, R.Z. Valiev, G. Wilde, M.J. Zehetbauer, X. Zhu, Nanomaterials by severe plastic deformation: review of historical developments and recent advances, Materials Research Letters 10(4) (2022) 163-256.
[32] Y. Huang, R.B. Figueiredo, T. Baudin, F. Brisset, T.G. Langdon, Evolution of Strength and Homogeneity in a Magnesium AZ31 Alloy Processed by High-Pressure Torsion at Different Temperatures, Advanced Engineering Materials 14(11) (2012) 1018-1026.
[33] F. Meng, J.M. Rosalie, A. Singh, H. Somekawa, K. Tsuchiya, Ultrafine grain formation in Mg–Zn alloy by in situ precipitation during high-pressure torsion, Scripta Materialia 78-79 (2014) 57-60.
[34] K. Bryła, J. Morgiel, M. Faryna, K. Edalati, Z. Horita, Effect of high-pressure torsion on grain refinement, strength enhancement and uniform ductility of EZ magnesium alloy, Materials Letters 212 (2018) 323-326.

[35] A. Hanna, H. Azzeddine, R. Lachhab, T. Baudin, A.-L. Helbert, F. Brisset, Y. Huang, D. Bradai, T.G. Langdon, Evaluating the textural and mechanical properties of an Mg-Dy alloy processed by high-pressure torsion, Journal of Alloys and Compounds 778 (2019) 61-71.
[36] R.B. Figueiredo, T.G. Langdon, Using High-Pressure Torsion to Achieve Superplasticity in an AZ91 Magnesium Alloy, Metals 10(5) (2020) 681.
[37] O. Ould Mohamed, H. Azzeddine, Y. Huang, T. Baudin, P. Bazarnik, F. Brisset, M. Kawasaki, T.G. Langdon, Investigation of Microstructure and Texture Evolution in an AZ31/Mg–Gd Alloy Hybrid Metal Fabricated by High-Pressure Torsion, Advanced Engineering Materials n/a(n/a) (2023) 2201794.
[38] R.Z. Valiev, Y.V. Ivanisenko, E.F. Rauch, B. Baudelet, Structure and deformaton behaviour of Armco iron subjected to severe plastic deformation, Acta Materialia 44(12) (1996) 4705-4712.
[39] D. Elfiad, Y.I. Bourezg, H. Azzeddine, D. Bradai, Investigation of texture, microstructure, and mechanical properties of a magnesium–lanthanum alloy after thermo-mechanical processing, nternational Journal of Materials Research 107(4) (2016) 315-323.
[40] K.D. Molodov, T. Al-Samman, D.A. Molodov, Effect of gadolinium on the deformation and recrystallization behavior of magnesium crystals, Acta Materialia 240 (2022) 118312.
[41] N. Stanford, M.D. Callaghan, B. de Jong, The effect of rare earth elements on the behaviour of magnesium-based alloys: Part 1—Hot deformation behaviour, Materials Science and Engineering: A 565 (2013) 459-468.
[42] N. Stanford, The effect of rare earth elements on the behaviour of magnesium-based alloys: Part 2 – recrystallisation and texture development, Materials Science and Engineering: A 565 (2013) 469-475.
[43] I. Basu, T. Al-Samman, Competitive twinning behavior in magnesium and its impact on recrystallization and texture formation, Materials Science and Engineering: A 707 (2017) 232-244.
[44] J.-f. Deng, J. Tian, Y. Zhou, Y. Chang, W. Liang, J. Ma, Plastic deformation and fracture mechanisms of rolled Mg-8Gd-4Y-Zn and AZ31 magnesium alloys, Materials & Design 223 (2022) 111179.
[45] C. He, J. Zhou, Y. Yang, B. Jiang, M. Yuan, Z. Dong, Y. Chai, W. He, G. Huang, D. Zhang, F. Pan, In-situ investigation on the microstructure evolution of Mg-2Gd alloys during the V-bending tests, Journal of Materials Science & Technology 131 (2022) 167-176.
[46] R.B. Figueiredo, P.R. Cetlin, T.G. Langdon, Using finite element modeling to examine the flow processes in quasi-constrained high-pressure torsion, Materials Science and Engineering: A 528(28) (2011) 8198-8204.
[47] H. Azzeddine, D. Bradai, T. Baudin, T.G. Langdon, Texture evolution in high-pressure torsion processing, Progress in Materials Science 125 (2022) 100886.
[48] F. Wetscher, A. Vorhauer, R. Stock, R. Pippan, Structural refinement of low alloyed steels during severe plastic deformation, Materials Science and Engineering: A 387-389 (2004) 809-816.
[49] J.-H. Cho, A.D. Rollett, K.H. Oh, Determination of a mean orientation in electron backscatter diffraction measurements, Metallurgical and Materials Transactions A 36(12) (2005) 3427-3438.
[50] R. Hielscher, H. Schaeben, A novel pole figure inversion method: specification of the MTEX algorithm, J. Appl. Cryst. 41(6) (2008) 1024-1037.
[51] O. Sitdikov, R. Kaibyshev, T. Sakai, Dynamic Recrystallization Based on Twinning in Coarse-Grained Mg, Materials Science Forum 419-422 (2003) 521-526.
[52] H.Z. Ye, X.Y. Liu, In situ formation behaviors of Al8Mn5 particles in Mg–Al alloys, Journal of Alloys and Compounds 419(1) (2006) 54-60.

[53] J.F. Nie, K.S. Shin, Z.R. Zeng, Microstructure, Deformation, and Property of Wrought Magnesium Alloys, Metallurgical and Materials Transactions A 51(12) (2020) 6045-6109.
[54] M. Nienaber, G. Kurz, D. Letzig, K.U. Kainer, J. Bohlen, Effect of Process Temperature on the Texture Evolution and Mechanical Properties of Rolled and Extruded AZ31 Flat Products, 12(9) (2022) 1307.
[55] M. Kawasaki, Different models of hardness evolution in ultrafine-grained materials processed by high-pressure torsion, Journal of Materials Science 49(1) (2014) 18-34.
[56] M. Kawasaki, R.B. Figueiredo, Y. Huang, T.G. Langdon, Interpretation of hardness evolution in metals processed by high-pressure torsion, Journal of Materials Science 49(19) (2014) 6586-6596.
[57] H.-J. Lee, S.K. Lee, K.H. Jung, G.A. Lee, B. Ahn, M. Kawasaki, T.G. Langdon, Evolution in hardness and texture of a ZK60A magnesium alloy processed by high-pressure torsion, Materials Science and Engineering: A 630 (2015) 90-98.
[58] B. Beausir, L.S. Tóth, K.W. Neale, Ideal orientations and persistence characteristics of hexagonal close packed crystals in simple shear, Acta Materialia 55(8) (2007) 2695-2705.
[59] K.E. Prasad, K.T. Ramesh, In-situ observations and quantification of twin boundary mobility in polycrystalline magnesium, Materials Science and Engineering: A 617 (2014) 121-126.
[60] Z.Y. Zhao, R.G. Guan, Y.F. Shen, P.K. Bai, Grain refinement mechanism of Mg-3Sn-1Mn-1La alloy during accumulative hot rolling, Journal of Materials Science & Technology 91 (2021) 251-261.
[61] T. Al-Samman, K.D. Molodov, D.A. Molodov, G. Gottstein, S. Suwas, Softening and dynamic recrystallization in magnesium single crystals during c-axis compression, Acta Materialia 60(2) (2012) 537-545.
[62] K.D. Molodov, T. Al-Samman, D.A. Molodov, G. Gottstein, Mechanisms of exceptional ductility of magnesium single crystal during deformation at room temperature: Multiple twinning and dynamic recrystallization, Acta Materialia 76 (2014) 314-330.
[63] D. Guan, W.M. Rainforth, L. Ma, B. Wynne, J. Gao, Twin recrystallization mechanisms and exceptional contribution to texture evolution during annealing in a magnesium alloy, Acta Materialia 126 (2017) 132-144.
[64] H. Azzeddine, Y.I. Bourezg, A.Y. Khereddine, T. Baudin, A.-L. Helbert, F. Brisset, M. Kawasaki, D. Bradai, T.G. Langdon, An investigation of the stored energy and thermal stability in a Cu–Ni–Si alloy processed by high-pressure torsion, Philosophical Magazine 100(6) (2020) 688-712.
[65] J.D. Robson, D.T. Henry, B. Davis, Particle effects on recrystallization in magnesium–manganese alloys: Particle-stimulated nucleation, Acta Materialia 57(9) (2009) 2739-2747.
[66] Y. Meng, J. Yu, K. Liu, H. Yu, F. Zhang, Y. Wu, Z. Zhang, N. Luo, H. Wang, The evolution of long-period stacking ordered phase and its effect on dynamic recrystallization in Mg-Gd-Y-Zn-Zr alloy processed by repetitive upsetting-extrusion, Journal of Alloys and Compounds 828 (2020) 154454.
[67] Q. Wu, H. Yan, J. Chen, W. Xia, M. Song, B. Su, The interactions between dynamic precipitates and dynamic recrystallization in Mg-5Zn-1Mn alloys during hot compression, Materials Characterization 160 (2020) 110131.
[68] J. Kacher, B.P. Eftink, B. Cui, I.M. Robertson, Dislocation interactions with grain boundaries, Current Opinion in Solid State and Materials Science 18(4) (2014) 227-243.